Speeding-up image-based simulation of two-phase flow in porous media with lattice-Boltzmann method using three-dimensional curvelet transforms



Speeding-up image-based simulation of twophase flow in porous media with lattice-Boltzmann method using three-dimensional curvelet transforms

Cite as: Phys. Fluids **33**, 113313 (2021); https://doi.org/10.1063/5.0065857 Submitted: 05 August 2021 • Accepted: 20 October 2021 • Published Online: 11 November 2021

Abdullah Aljasmi and D Muhammad Sahimi







Physics of Fluids

SPECIAL TOPIC: Flow and Acoustics of Unmanned Vehicles



Submit Today!

Speeding-up image-based simulation of two-phase flow in porous media with lattice-Boltzmann method using three-dimensional curvelet transforms

Cite as: Phys. Fluids 33, 113313 (2021); doi: 10.1063/5.0065857 Submitted: 5 August 2021 · Accepted: 20 October 2021 · Published Online: 11 November 2021







Abdullah Aljasmi and Muhammad Sahimi^{a)} 🕞



AFFILIATIONS

Mork Family Department of Chemical Engineering and Materials Science, University of Southern California, Los Angeles, California 90089-1211, USA

Note: This paper is part of the Special Issue on the Lattice Boltzmann Method. ^{a)}Author to whom correspondence should be addressed: moe@usc.edu

ABSTRACT

Multiphase fluid flow in porous media is relevant to many fundamental scientific problems as well as numerous practical applications. With advances in instrumentations, it has become possible to obtain high-resolution three-dimensional (3D) images of complex porous media and use them directly in the simulation of multiphase flows. A prime method for carrying out such simulations is the color-fluid lattice Boltzmann method with multirelaxation time (CFLB-MRT) collision operator. The simulations are, however, time consuming and intensive. We propose a method to accelerate image-based computations with the CFLB-MRT method, in which the 3D image is preprocessed by curvelet transforming it and eliminating those details that do not contribute significantly to multiphase flow. The coarsening is done by thresholding the image. After inverting the coarser image back to the real space, it is utilized in the simulation of multiphase flow by the CFLB-MRT approach. As the test of the method, we carry out simulation of a two-phase flow problem in which the porous media are initially saturated by brine or water, which is then displaced by CO₂ or oil, injected into the pore space. The simulations are carried out with two types of sandstone. We show that the method accelerates the computations significantly by a factor of up to 35.

Published under an exclusive license by AIP Publishing. https://doi.org/10.1063/5.0065857

I. INTRODUCTION

Porous media and materials are ubiquitous. They range anywhere from large-scale porous formations, such as soil, sandpiles, oil, gas, and geothermal reservoirs, and groundwater aquifers, to those that are present in everyday life, such as sponge, textile, printing paper, biological tissues, wood, pavement, and asphalt. Practically all the natural porous media and a large class of man-made ones are heterogeneous, with the heterogeneity manifesting itself over a range of length scales, from the pore to core and field scale. Of particular interest is understanding how fluid flow and transport processes occur in the pore space of porous media and materials. Aside from experimental studies of such phenomena that have been undertaken for at least two centuries, characterization of porous media and materials and modeling of various phenomena in them have also been studied for decades.

To carry out theoretical and computational studies of various phenomena in a porous medium, one requires, as a first step, a representative model of its pore space. The earliest theoretical studies of fluid flow and transport in porous media were based on the assumption that they could be represented as continua to which effective flow and transport properties, such as the permeability and diffusivity were attributed and, thus, the governing equations describing the phenomena of interest in such continua were solved. The effective properties were either measured or estimated by simple models, such as bundles of parallel capillary tubes.² Since such models proved inadequate, beginning with the work of Meyer³ and Fatt, 4,5 more advanced models of pore space in the form of networks of interconnected pores began to emerge. Although due to the computational limitations, early pore-network models (PNMs) were relatively limited and provided mostly qualitative insights into the phenomena under study, with advances in computational power, the PNMs gradually became quantitative and are still used in the study of many phenomena in porous media and materials.6

However, even the most accurate PNMs are constructed based on a number of assumptions, such as how the pore throats and pore bodies are defined, the manner by which sizes are attributed to both, and where a pore throat ends and a pore body begins. On the other hand, with significant advances in instrumentation, one can obtain high-resolution two- or three-dimensional (3D) images of porous media that are important, not only for their characterization, 9the detailed information that they provide for the morphology, but also for modeling of fluid flow and transport through them. The only constraint for using the images in the computations is that their physical size must be larger than that of the representative elementary volume (REV), the minimum size of a porous medium whose properties are independent of its dimensions. In other words, the REV is the smallest volume of the porous medium over which a measurement can be made that will yield a representative value of the entire porous medium. Thus, use of high-resolution images in the numerical simulations of fluid flow in porous media is becoming more common. They have been used for computing the elastic properties of porous media, the permeability, 11-17 simulation of two-phase flow, 18,19 and adsorption and deformation²⁰ in porous materials.

If an image is to be used in the numerical simulation of fluid flow (and other phenomena for that matter), one must select a suitable numerical method for solving the governing equations. One method for doing so is based on solving the governing equations—the mass conservation and Stokes' equations—in the image by the finite-element or finite-volume, and particularly the boundary singularity method. A second popular approach is based on the lattice-Boltzmann (LB) method^{21–24} that solves the discrete Boltzmann equations. The method is based on streaming, collision, and relaxation of a set of fluid particle distribution functions (PDFs) on a lattice. Provided that the lattice has enough symmetry, the discrete equations reduce in the continuum limit to the Stokes' or the Navier–Stokes equations.

Whether one solves the governing equations directly, or utilizes the LB method, the computations are intensive, particularly when the image is in 3D and has high resolution. Thus, one tries to coarsen the image in order to reduce the computations times. Several methods have been proposed^{25–27} by computer scientists for image coarsening. In addition, when computational fluid dynamics is used to study fluid flow in images of various types of systems, such as images obtained by

magnetic resonance techniques, the image is also coarsened, and then the effect of the coarsening level on the accuracy of the results is studied. ^{28,29}

In this paper, we propose a novel method for image-based numerical simulation of two-phase flow in porous media using the LB method, whereby the image is first processed with 3D curvelet transforms (CTs) in order to develop a coarse, yet accurate image of the pore space. We show that the results of numerical simulation of twophase flow in the coarsened image are as accurate as those obtained by using the original high-resolution image, while the computations' time is reduced by one order of magnitude or better. To our knowledge, the CTs have never been used for coarsening of complex images for use in the study of fluid dynamical phenomena. While as discussed below, wavelet transformations have been used for coarsening of computational grids, the images of heterogeneous porous media are highly complex, with the pores and the interface between them and the solid matrix of porous media being oriented in all directions, which cannot be accounted for by the wavelet and similar transformations, nor by almost all other coarsening methods. The CTs, having an orientational variable (see below) θ , can account for the orientation effect. We are aware of no other method that has such a property.

The rest of this paper is organized as follows. In Sec. II, we briefly describe the 3D porous media that we use in the simulations. Section III explains the 3D CTs and their properties. In Sec. IV, the LB method used for simulating the two-phase flow problem is described. Processing of the 3D image of the porous media by CTs is explained in Sec. V. The results are presented and discussed in Sec. VI. Section VII presents a summary of the paper.

II. THE POROUS MEDIA

We simulated two-phase flow in the 3D image of two porous media. One was a Berea sandstone, a benchmark for testing accuracy and efficiency of various computational approaches to numerical simulation of multiphase flows in porous media. $^{30-32}$ The resolution of the scan was $10.7~\mu m$, while the sample's physical size was $2.14^3~mm^3$, with the size of its digitized image being 200^3 voxels. Since the porosity of the sample is about 0.2, then, roughly speaking, about 1.6×10^6 voxels are present in the pore space; see Table I that also presents the basic physical properties of the sandstone. The 3D image of the sandstone is shown in Fig. 1.

TABLE I. Comparison of the physical properties of three porous media before and after they are processed by curvelet transformation and their dependence on the threshold ϵ .

Berea sandstone	3	Permeability (mD)	Porosity (%)	Pore surface area (nm²)
Original image		1273	1273 19.63 189.74	
Curvelet-processed image	0.5	1356	20.54	196.31
Curvelet-processed image	0.9	1383	21	199.22
Regenerated sandstone				
Original Image		125	18.36	44.11
Curvelet-processed image	0.5	131	19.12	46.45
Curvelet-processed image	0.9	134	19.77	47.23
Carbonate				
Original image		5.54	43.00	1.94
Curvelet-processed image	0.5	5.74	44.13	2.01
Curvelet-processed image	0.9	5.78	44.54	2.06

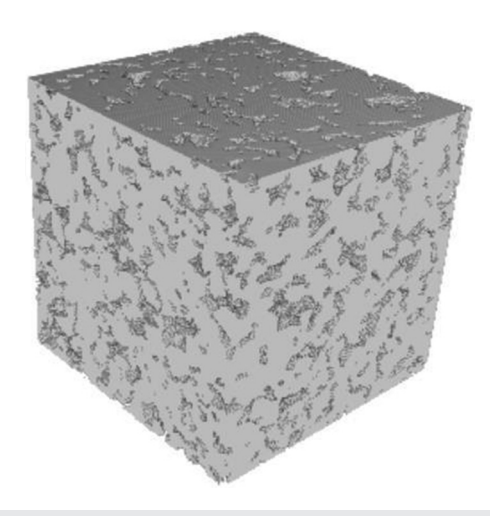


FIG. 1. The image of the Berea sandstone used in the simulations.

The second porous medium in which we simulated two-phase flow was also a sandstone, originally developed by An *et al.*^{33,34} They drilled a cylindrical core plug from a sample whose length and diameter were, respectively, 4 cm and 10 mm. Its image, obtained by x-ray, was then digitized, and a section of it with 256³ voxels was used in their simulations. An *et al.*³³ showed that the size of the sample was larger than the REV. Figure 2 presents its 3D image, while its basic properties are also listed in Table I. Following An *et al.*,^{33,34} we refer to this porous medium as the regenerated sandstone; see Table I.

The third image with a size of 512² pixels was from a fossiliferous outcrop carbonate, Mt. Gambier limestone in South Australia with porosity of 0.43. The physical size of the image was 2.76 mm². Figure 3 shows the image. Its physical properties are listed in Table I. Since we previously carried out simulation of two-phase flow in this image,¹⁹ we only analyzed its main properties under the CT and coarse-graining, which will be described shortly.



FIG. 2. The image of the regenerated sandstone utilized in the simulations.

III. THREE-DIMENSIONAL CURVELET TRANSFORMS

Although the original CTs that were developed for image processing were two dimensional, ^{35,36} there are many scientific problems and engineering applications, such as processing of 3D seismic and medical images, which motivated the development of 3D CTs, particularly because they preserve the important features of complex 3D systems, which is why their use is becoming more common.

Three-dimensional CTs are constructed in a manner similar to their 2D counterparts. Thus, in continuous CTs, a frequency window $\hat{U}_j(r,\omega)$ is constructed by introducing two other windows. One is a radial window W(r), defined by 37,38

$$\sum_{j=-\infty}^{\infty} W^2(2^{-j}r) = 1, \tag{1}$$

which smoothly extracts the frequency near the wedge, $\{2^{j-1} \le r \le 2^{j+1}\}$, with r being the polar coordinate. The second window $V(\theta)$ is defined by 37,38

$$\sum_{j=-\infty}^{\infty} V^2(\theta - 2j) = 1, \quad \theta \in \mathcal{R}, \tag{2}$$

implying that for each scale j a unit sphere S^2 , representing all the orientations in \mathcal{R}^3 , is considered and is partitioned into $\mathcal{O}(2^{j/2}\times 2^{j/2})=\mathcal{O}(2^j)$ smooth angular windows $V(\theta)$ with a circular support of radius $\mathcal{O}(2^{-j/2})$, the squares of which form a partition of unity on S^2 . The window $U_j(r,\theta)$ is then defined by 37,38

$$U_j(r,\theta) = \frac{1}{2\pi} 2^{3j/4} W(2^{-j}r) V(2^{[j/2]}\theta). \tag{3}$$

Here, $[\cdot]$ denotes the integer part of the number. Then, $\hat{U}_j(\boldsymbol{\omega})$ is simply the Fourier transform of $U_j(r, \theta)$.

The mother curvelet $\phi_i(\mathbf{x})$, based on which all other curvelets at scale 2^{-j} , are constructed by rotation and translation of $\phi_i(\mathbf{x})$, is defined by, $\hat{\phi}_i(\boldsymbol{\omega}) = \hat{U}_j(\boldsymbol{\omega})$. The 3D curvelets are defined as a function of $\mathbf{x} = (x_1, x_2, x_3)$ at scale 2^{-j} , orientation $\theta_{j,l}$, and position $\mathbf{x}_k^{(j,l)} = \mathbf{R}_{\theta_{j,l}}^{-1}(k_1 \times 2^{-j}, k_2 \times 2^{-j/2}, k_3 \times 2^{-j/2})$, i.e., $\phi_{j,l,k}(\mathbf{x}) = \phi_j[\mathbf{R}_{\theta_{j,l}}(\mathbf{x} - \mathbf{x}_k^{(j,l)})]$, where (k_1, k_2, k_3) are translation parameters, and $\mathbf{R}_{\theta_{j,l}}$ is the rotation by the angle $\theta_{j,l}$, 37,38

$$\mathbf{R}_{\theta_{j,l}} = \begin{pmatrix} \cos \theta_{j,l} & \sin \theta_{j,l} \\ -\sin \theta_{j,l} & \cos \theta_{j,l} \end{pmatrix}. \tag{4}$$

Suppose that a 3D image of a porous medium, an $n \times n \times n$ array of voxels, is represented by $\mathcal{I}(\mathbf{x})$. Then, its CT, usually referred to as the *curvelet coefficients* (CCs) $\mathcal{C}_{j,l,k}$ of \mathcal{I} , is defined by³⁷

$$C_{j,l,k} == \int \mathcal{I}(\mathbf{x}) \overline{\phi_{j,l,k}(\mathbf{x})} \, d\mathbf{x}, \tag{5}$$

which, after using the Plancherel's theorem, is rewritten in the frequency space,³⁷

$$C_{j,l,k} := \frac{1}{(2\pi)^3} \int \hat{\mathcal{I}}(\boldsymbol{\omega}) \overline{\phi_{j,l,k}^{\hat{i}}}(\boldsymbol{\omega}) d\boldsymbol{\omega}$$

$$= \frac{1}{(2\pi)^3} \int \hat{\mathcal{I}}(\boldsymbol{\omega}) U_j(R_{\theta l} \boldsymbol{\omega}) \exp\left(i \langle \mathbf{x}_k^{j,l}, \boldsymbol{\omega} \rangle\right) d\boldsymbol{\omega}, \tag{6}$$

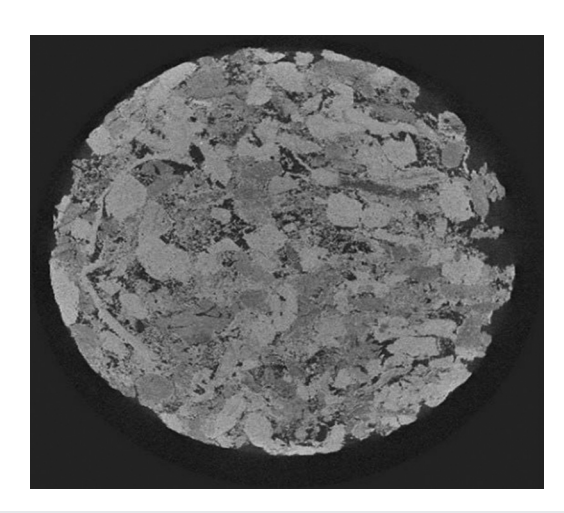


FIG. 3. The image of the carbonate porous medium analyzed by curvelet transformation

where the overline denotes the complex conjugate.

Since the digitized images of porous media are discrete, we need to rewrite the above formulation in discrete form. The 3D discrete CT operates on a 3D Cartesian grid—the 3D image $\mathcal{I}(n_1, n_2, n_3)$ of the medium with $0 \le (n_1, n_2, n_3) \le n$ —and generates a set of the CCs $\mathcal{C}^D(j, l, k)$ that are defined by 37,38

$$C^{D}(j,l,k) = \sum_{n_1} \sum_{n_2} \sum_{n_3} \mathcal{I}(n_1, n_2, n_3) \overline{\phi_{j,l,k}^{D}(n_1, n_2, n_3)}, \quad (7)$$

with $(j,l) \in Z$ and $k = (k_1,k_2,k_3)$. Since, as described below, by curve-transforming of an image we obtain a new coarse-scale image, we also need to consider the coarser scales. Thus,³⁷ suppose that the frequency window \hat{U}_{s_0} at scale $j = s_0$ in a rectangular box of integer size, $L_{1,s_0} \times L_{2,s_0} \times L_{3,s_0}$, is defined by the usual relation, $\hat{U}_{s_0,0}(\omega) = \hat{W}_{s_0}(\omega)$. Then, the 3D discrete curvelets at the coarsest scale are defined by their Fourier transform,³⁷

$$\hat{\phi}_{s_0,0,k}^D(\omega) = \frac{1}{N} \hat{U}_{s_0,0}(\omega) \exp[-2\pi i (k_1 \omega_1 / L_{1,s_0} + k_2 \omega_2 / L_{2,s_0} + k_3 \omega_3 / L_{3,s_0})], \tag{8}$$

where N is given by 37

$$N = (L_{1,s_0} L_{2,s_0} L_{3,s_0})^{1/2}, (9)$$

for $0 \le k_1 < L_{1,s_0}$, $0 \le k_2 < L_{2,s_0}$, and $0 \le k_3 < L_{3,s_0}$.

On the other hand, for the fine scales $s_0 < j$, every Cartesian funnel-shaped region has six components, one for each face of the unit cube and is partitioned into $2^{j/2} \times 2^{j/2} = 2^j$ same-volume wedges. For example, suppose that for the *l*th wedge in the first component, $(1, \alpha_l, \beta_l)$ indicates the direction of the centerline of the wedge. Then, an angular window is defined by³⁷

$$\tilde{V}_{j,l}(\boldsymbol{\omega}) = \tilde{V}\left(2^{j/2} \times \frac{\omega_2 - \alpha_l \omega_1}{\omega_1}\right) \tilde{V}\left(2^{j/2} \times \frac{\omega_3 - \beta_l \omega_1}{\omega_1}\right), \quad (10)$$

with V given by Eq. (2). Similar definitions hold for the other five components by exchanging the roles of ω_1 with ω_2 or ω_3 . Then, the

frequency window $\hat{U}_{j,l}$ is defined by $\hat{U}_{j,l}(\omega) = \hat{W}_j(\omega)\hat{V}_{j,l}(\omega)$, which isolates the frequencies near the wedge $\{(\omega_1,\omega_2,\omega_3): 2^{j-1} \leq \omega_1 \leq 2^{j+1}, -2^{-j/2} \leq \omega_2/\omega_1 - \alpha_l \leq 2^{-j/2}, -2^{-j/2} \leq \omega_3/\omega_1 - \beta_l \leq 2^{-j/2}\}$. Then, $\hat{\phi}_{j,l,k}^D(\omega)$, the discrete curvelet at the fine scales $s_0 < j$ with index k at scale j and angle l is defined in a manner similar to Eq. (8), but with L_{i,s_0} replaced by $L_{i,j,l}$ with i=1,2, and 3.

Figure 4 summarizes the discussions. Figure 4(a) presents schematically the 2D spatial Cartesian grid associated with a given scale and orientation. Figure 4(b) shows the corresponding partitioning of the frequency domain as a result of Cartesian grid shown in Fig. 4(a). As shown, the 2D curvelets in the Fourier space are supported near "parabolic" wedge shown generically by the shaded area. Likewise, Fig. 4(c) shows the schematically the frequency tiling of continuous 3D curvelets, while Fig. 4(d) depicts discrete frequency griding, with ω_1, ω_2 , and ω_3 being the three frequency axes. As described above, the frequency window $\hat{U}_{j,l}(\omega)$ extracts the frequency content near the shaded wedge that has center slope (l, α_l, β_l) . Note that it is precisely the ability of partitioning in the frequency domain along various orientations that makes the curvelet the ideal tool for pre-processing of an image with complex features that may be oriented stochastically in space.

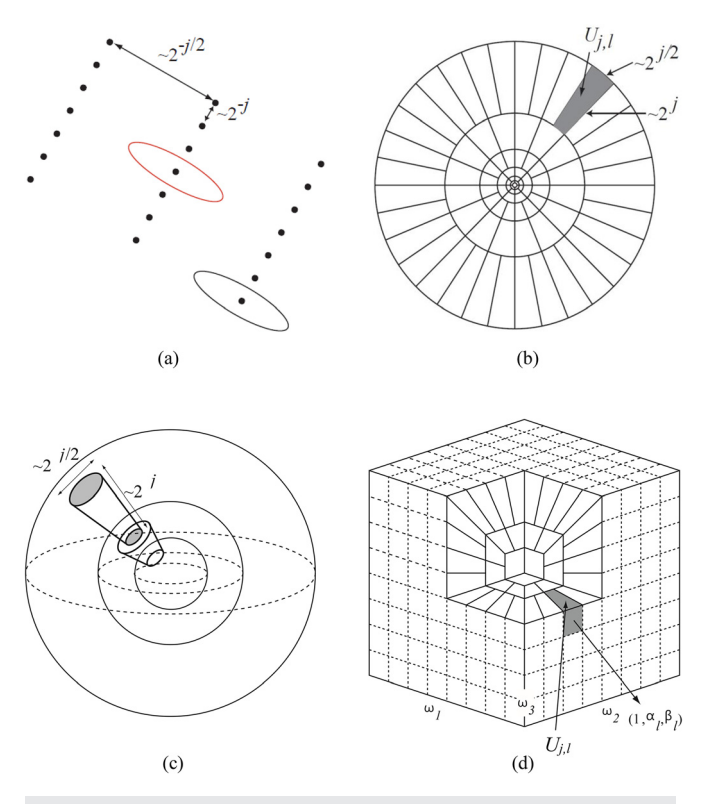


FIG. 4. (a) Schematic representation of the Cartesian grid associated with a given scale j and orientation. (b) The corresponding partitioning of the frequency domain. Shaded wedge indicates the region in which the 2D curvelets in Fourier space are supported. The corresponding 3D structures are shown in (c) and (d), with (c) showing the schematic representation of tiling of 3D continuous curvelets, whereas (d) shows the discrete tiling in the frequency domain (after Ying et al.

IV. THE LATTICE-BOLTZMANN METHOD

To simulate the two-phase flow problem, we used the color-fluid lattice Boltzmann (CFLB) multiphase simulator developed by Chen et al., 39 which is a variant of the original work of Gunstensen et al. 40 and Tölke et al. 41 The method produces a relatively sharp interface between completely immiscible fluids, as well as being capable of simulating two-phase flows with large ratios of the two fluids' viscosities, which is a difficult problem since large viscosity ratios give rise to unstable displacements and fingering phenomena. The ability of the method for accurate simulation of such phenomena is due to the independent control of the surface tension and viscosity, which is why it has been widely adopted; see, for example, Ahrenholz et al. 42

In the CFLB model, one labels the various fluids with color. Thus, let red (r) and blue (b) represent the two fluids in a two-phase system. The two fluids are represented by their own particle distribution functions (PDFs) $f_i^r(\mathbf{x},t)$ and $f_b^i(\mathbf{x},t)$ in the ith direction of the lattice. We used the 3D LB model with 19 discrete velocities, i.e., the D3Q19 model. The overall PDF for the fluid system at position \mathbf{x} at time t is given by $f_i(\mathbf{x},t) = f_i^r(\mathbf{x},t) + f_i^b(\mathbf{x},t)$, where

$$f_i^c(\mathbf{x} + \mathbf{v}_i^c \Delta t, t + \Delta t) = f_i^c(\mathbf{x}, t) + \Omega_i^x(\mathbf{x}, t), \quad i = 0, 1, 2, \dots, 18.$$

$$(11)$$

Here, superscript c denotes the colors (c=r,b), \mathbf{v}_i^c represents the discrete velocities, and $\Omega_i^c(\mathbf{x},t)$ is the usual collision operator, given by $^{43-45}$

$$\Omega_i^c = \Omega_i^{c(3)} \Big[\Omega_i^{c(1)} + \Omega_i^{c(2)} \Big], \tag{12}$$

where $\Omega_i^{c(1)}$ is the standard LB single relaxation time collision operator, 39,40

$$\Omega_i^{c(1)} = -\left(\frac{1}{\tau^c}\right) \left[f_i^c - f_i^{c,eq}\right],\tag{13}$$

with τ^c being the relaxation parameter. $\Omega_i^{c(2)}$ is the perturbation operator that generates surface tension, while $\Omega_i^{c(3)}$ represents the "recoloring" that mimics the separation of the two fluids (recall that the two fluids are represented by two distinct colors). The macroscopic variables are given by the standard expressions, namely, $\rho_r = \sum_i f_i^r$, $\rho_b = \sum_i f_i^b$, $\rho = \rho_r + \rho_b$, and $\rho \mathbf{v} \sum_i f_i \mathbf{e}_i$, for, respectively, the densities of the red and blue fluids, the overall density, and the momentum, with $\mathbf{v} = (v_x, v_y, v_z)$ being the fluid velocity vector. The pressure p is then given by $p = |\mathbf{v}|^2 \rho/3$, where $\mathbf{v} = \Delta \mathbf{x}/\Delta t$ is the speed,

The operator $\Omega_i^{c(2)}$ is given by⁴¹

$$\Omega_i^{c(2)} = A_{\sigma} |\mathbf{C}| \left[\frac{(\mathbf{v}_i^c \cdot \mathbf{C})^2}{\mathbf{C}^2} - \frac{5}{9} \right], \tag{14}$$

with the free parameter A_{σ} being proportional to the interfacial tension σ . The same collision operator was used for both fluids. The color gradient ${\bf C}$ is given in the Appendix. The recoloring collision step redistributes $f_i^{c,(2)}$ to achieve separation of the two fluids, ⁴³ where $f_i^{c,(2)}$ is the distribution function after applying the second operator. The step is represented by the following maximization problem: ^{41,46}

$$\max_{f_i^{r,(3)}} \mathbf{C} \cdot \sum_i \mathbf{v}_i^r f_i^{r,(3)}. \tag{15}$$

In practice, this is done numerically.⁴³

It is well-known⁴⁷ that a barrier to the stability of the LB simulation is the presence of oscillations in the vicinity of sharp gradients in the flow, which may be caused by, for example, the no-slip boundary condition on the solid surface. Such oscillations are common in discrete approximations of continuous equations. This is particularly so for two-phase flow in porous media. To address this issue, a multirelaxation time (MRT) operator, proposed by d'Humieres *et al.*⁴⁸ and Lallemand and Luo⁴⁹ is used, since it helps to suppresses the oscillations. Thus, we utilized the MRT collision operator in which the post-collision bulk PDF is given by⁴⁸

$$f_i^p(\mathbf{x},t) = f_i(\mathbf{x},t) - \mathbf{M}^{-1}\mathbf{S}(\mathbf{Mf} - \mathbf{m}^{\text{eq}}), \quad i = 0, 1, ..., 18,$$
 (16)

where **M** is the matrix that transforms **f** to the momentum space, and **S** is the diagonal matrix of the relaxation rates S_{ii} . The size of both matrices is 19×19 . The vector \mathbf{m}^{eq} denotes the equilibrium state of the moments $\mathbf{m} = \mathbf{M}\mathbf{f}$ of the PDF, with **M** given by d'Humieres $et\ al.,^{47}$ and presented in the Appendix for completeness. The nineteen entries of \mathbf{m}^{eq} , as well as the diagonal matrix **S**, which were also given by d'Humieres $et\ al.,^{47}$ are also quoted in the Appendix for completeness.

Since the two fluids whose flow we simulate are immiscible, the effect of the surface tension σ , as well as the contact angle θ , must be taken into account. An order parameter ϕ is defined by

$$\varphi = \frac{\rho_r - \rho_b}{\rho_r + \rho_b}.\tag{17}$$

To include the effect of the contact angle, the value of the order parameter φ on the solid boundaries of the porous medium is set to be⁵⁰ $\varphi = \cos \theta$. Then, additional terms \mathbf{m}^s are added to the stress-related entries of the equilibrium moments \mathbf{m}^{eq} . The nonzero entries of \mathbf{m}^s are given in the Appendix. Finally, the effective viscosity μ_e of the mixture is taken to be

$$\frac{1}{\mu_e} = \frac{1+\varphi}{2\mu_r} + \frac{1-\varphi}{2\mu_b}.$$
 (18)

One of the main characteristic quantities of any two-phase flow is the relative permeabilities of the two fluids. The relative permeability of a fluid phase α is the ratio of the permeability of that part of the pore space occupied by α and the single-phase permeability K_e of the entire pore space. To begin the LB simulation and compute the relative permeabilities, we utilized the steady-state method in which a predefined fractional flow of both fluid phases is injected into the pore space at constant flow rates, while the pressure in the opposite face of the sample is constant. Steady state is deemed to have been reached when the downstream and upstream fractional flows are equal.

To specify the predefined fractional flow in the LB method, an initial distribution of the two fluids in the pore space at a given value of the saturation is imposed, after which the LB simulation determines the actual spatial distribution of the two fluids at that saturation. The input geometry is mirrored and periodic boundary conditions along the direction of macroscopic flow are also imposed in order to allow both fluid phases enter and exit the model smoothly. In addition, a body force is applied to each fluid phase to achieve the same pressure drop and avoid capillary end effects. The volume flow rates of both phases are monitored in order to ensure that they converge to the true

steady state, which are then used to compute the relative permeability at the target saturation.

V. PROCESSING OF THE THREE-DIMENSIONAL IMAGES OF POROUS MEDIA

The morphology of natural porous media is not completely random, but contains extended spatial correlations even at the pore and grain scale. ⁵¹ Thus, the voxels in a 3D image of a porous medium are also correlated with the same type of correlation function. If the correlations are positive, which they usually are, then the images contain regions with similar properties. As a result, one does not need resolved lattice structure in such regions, and use of a coarser lattice would not distort the accuracy of the simulations. As we demonstrate shortly, this is indeed the case.

To implement the pre-processing of the image prior to the twophase flow simulation, we exploit the fact that ⁵² the CCs represent a measure of the local complexity of an image of a porous medium between the pores, as well as between them and the solid matrix through the pores' rough surface, such that the larger the CCs, the more significant are the correlations and the local complexity of the pore space, as well as their contribution to the image-based simulation of multiphase flow. Thus, by preserving only the most important parts of the pore space based on the CCs, a coarser computational grid should suffice for the simulations.

To coarsen the image we use a simple approach, which is used widely in image processing and is referred to as *thresholding*. It consists of the following steps:

- The image of the porous medium is first curvelettransformed and the CCs are computed.
- (ii) The largest CC is identified and all the computed CCs are normalized with respect to the largest value, so that they are all in the interval (0,1].
- (iii) A threshold $0 \le \varepsilon < 1$ is introduced, and all the CCs are examined one by one. If a CC $\mathcal{C}_{j,l,k}$ is smaller than ε , the set threshold, it is set to zero. Thus, the pre-processing generates a sparser representation of the image in the curvelet space because many of the CCs of the original image are set to zero.
- (iv) After step (iii) is completed, the CT of the image in which many of the CCs are zero is inverse curvelet-transformed and is brought back to the real space. The result is a coarsened image of the original image.

Other methods of compression to develop a coarser image with the CTs have also been developed. 25,27,53

Before presenting the results, we point out that there are very good o pen-source toolbox for image processing with the CTs, ⁵⁴ which can be used in the type of problems that we discuss in the present paper.

VI. RESULTS AND DISCUSSION

We simulated two-phase flow in which the porous medium was initially saturated by brine or water, and CO_2 or oil was injected into the pore space at one face with a constant injection speed v to displace the brine or water, while the pressure was specified on the opposite face. No-flow boundary condition was used in the remaining four faces of the 3D images. The capillary number in both simulations was

Ca = $\mu v/\sigma=10^{-4}$, corresponding to slow, capillary-dominated displacement, with μ and σ being, respectively, the viscosity and interfacial tension. The ratio of viscosities of the two fluids was 10, corresponding to an unstable displacement. For the CO₂-brine system, the interfacial tension was assumed to be $\sigma=30\,\mathrm{mN/m}$; see below for the second two-phase flow system. The two sandstones in which the two-phase flow problem was simulated are brine- or water-wet; therefore, the contact angle for CO₂ and oil was assumed to be 180°, although, as described earlier, any other contact angle can be implemented. All the computations were carried out on a HP Specter x360 laptop with speed of 2 GHz and 16 GB of memory.

In what follows, we present and discuss the results.

A. Properties of porous media under curvelet transformation

To see how the essential features of the porous media are preserved after being processed by the CTs, consider, first, the image shown in Fig. 5(a), which is that of a tight porous medium dominated by fractures. The image was processed by the CT with a threshold, $\varepsilon=0.8$. The resulting image is shown in Fig. 5(b). All the essential features of the medium, including the connectivity of the fractures that plays the most important role in fluid flow in the porous medium, are preserved, even though the threshold is very large.

Although Fig. 5 indicates clearly that the essential features of the image are preserved after coarsening, we also address the question of whether any important physical property of the porous media that we process, such as the porosity, pore surface area, and others, are also preserved under curvelet thresholding. To address this issue, we computed the porosity, single-phase permeability, and pore surface area of the original two sandstones, as well as those of the carbonate sample. After thresholding their images by the CT, we recomputed the same properties. To compute the pore surface area, we utilized the open-source Fiji software. First, we input the image into the software and converted it to a binary image. Next, we applied a threshold such that only the pores were shown and the solid matrix was covered. We then used the analysis tool of the software to compute the pore space internal surface area. The results are listed in Table I.

In the case of the Berea sandstone, even with a threshold as high as $\varepsilon = 0.9$ (recall that the maximum value of ε is 1), the effective permeability K_{ε} differs from that of the original porous medium by only

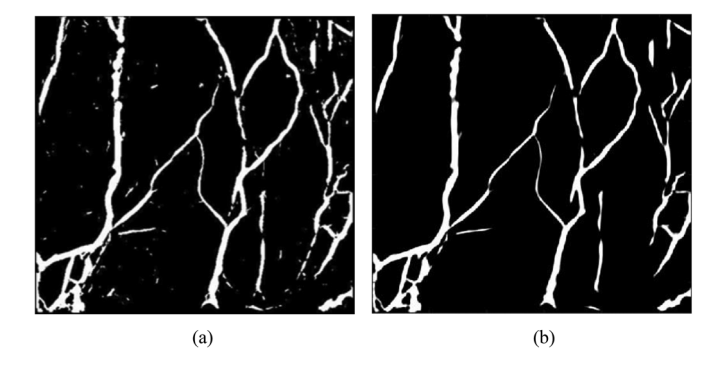


FIG. 5. Comparison of the original rock sample (a) with its thresholded version (b), obtained with a threshold $\varepsilon=0.8$. Observe that all the essential features are preserved under thresholding.

8% (see Sec. VIB below for the details of computing K_e). The corresponding differences for the porosity and pore surface area are, respectively, 6.9% and 5%. As we describe below, such a high threshold results in tremendous reduction in the overall computation time. The same type of observations may be made regarding the other two porous media that we consider. For example, with a threshold, $\varepsilon = 0.9$, the permeabilities of the curvelet-processed images of the regenerated sandstone and the carbonate sample differ from their original values by, respectively, only 6.4% and 4.3%.

We also computed a multiple-point connectivity function $p(\mathbf{h}; m)$ that quantifies the long-range connectivity of a porous material. $p(\mathbf{h}; m)$ is the probability of having a sequence of m connected points in the pore space of a porous material in a specific direction \mathbf{h} and is defined by

$$p(\mathbf{r}; m) = \text{Prob}[I(\mathbf{x}) = 1, I(\mathbf{x} + \mathbf{h}) = 1, ... I(\mathbf{x} + m\mathbf{h}) = 1], (19)$$

where $I(\mathbf{x})$ is the indicator function, i.e., $I(\mathbf{x}) = 1$ if \mathbf{x} is in the pore space, and $I(\mathbf{x}) = 0$, otherwise. Note that $p(\mathbf{h}; m)$ accounts for curvilinearity and complexity of a microstructure since it represents the probability of finding multiple connected points in such complex media. As such, it provides a stringent test of preserving the essential features of the image under CTs.

We computed $p(\mathbf{h}; m)$ for the two sandstones. Figure 6 shows the results for the Berea sandstone, and its curvelet-processed images. As can be seen, there is hardly any difference between the original image and the processed ones. Similar results were obtained for the regenerated sandstone. We conclude, therefore, that all the essential properties of the pore space are preserved under curvelet transformation.

B. Berea sandstone

We first determined the minimum lattice size for the CFLB simulations that would yield an effective single-phase permeability K_e that will not change if the resolution of the lattice was increased and a

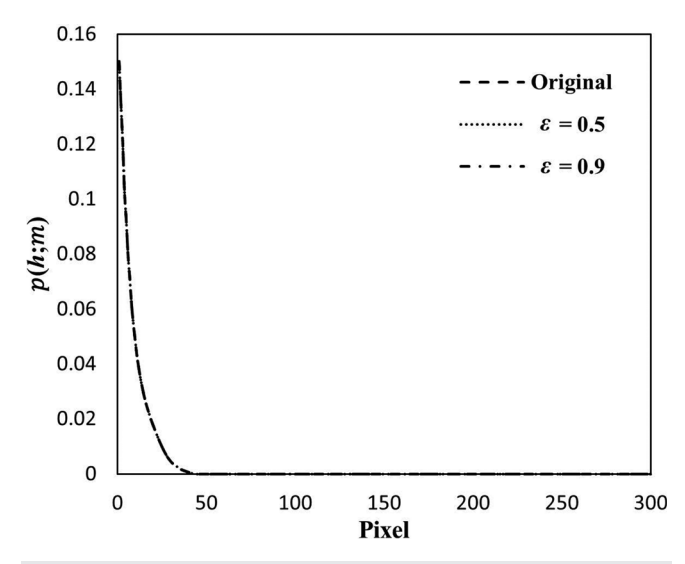


FIG. 6. The connectivity function $p_{(\mathbf{h}:m)}$ computed for the Berea sandstone, and its two coarsened versions, with m=100.

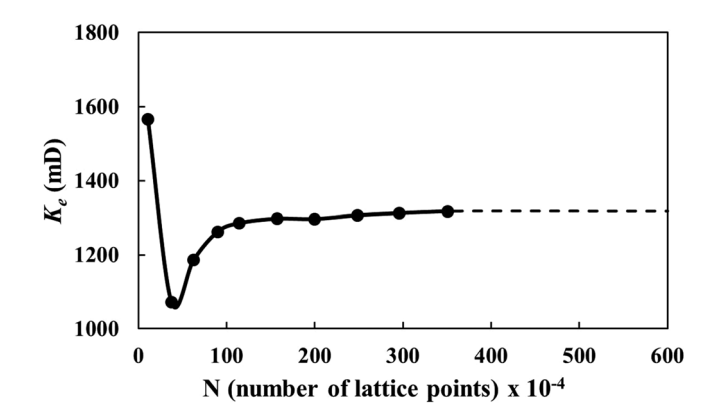


FIG. 7. Dependence of the permeability of the Berea sandstone on the number of the lattice nodes N in the LB simulation.

larger number of lattice nodes were used. To do so, we computed the dependence of K_e on the lattice size. Figure 7 presents the results, indicating that the Q19 lattice with about 1.69×10^6 lattice points produces effective permeability that is independent of the size. The same lattice was then used in the simulation of two-phase flow. To estimate the speed-up in the computations, we carried out the same detailed simulations in the original image and in two coarser ones obtained by thresholding the image with $\varepsilon=0.5$ and 0.9.

In Fig. 8, we compare the spatial distribution of CO_2 and brine in the original image of the sandstone with those obtained with the CT-processed images with the two thresholds. The brine saturation is $S_b = 0.5$. All the important features of three distributions are completely similar.

To make a quantitative comparison between the results obtained with the three images, we compare in Fig. 9 the saturation profile of CO_2 along the macroscopic direction x of the flow of CO_2 at its breakthrough time t_B , i.e., the time at which CO_2 -filled pores form a sample-spanning cluster across the image. In Fig. 9, X = x/L, where L is the linear size of the image, and the saturation $S_{CO_2}(X)$ was computed in the planes perpendicular to the macroscopic direction at X. The agreement between the three sets of results is excellent.

We make another quantitative comparison between the three sets of results in Fig. 10, where we show the time-dependence of CO_2 saturation $S_{CO}2$ in the original image of the porous medium and those computed with the thresholded images. In Fig. 10, $t_D = t/t_s$, where t

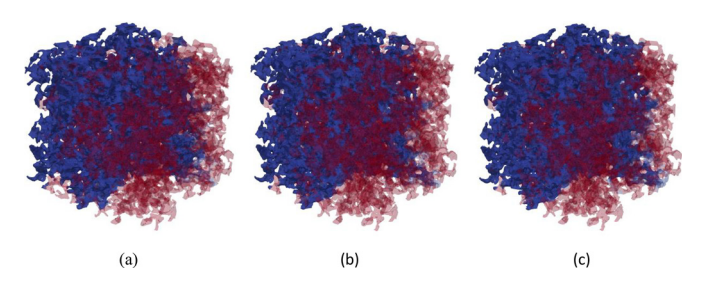


FIG. 8. CO₂ invasion patterns in the Berea sandstone. (a) The original image; (b) in the thresholded image with $\varepsilon=0.5$ image, and (c) in thresholded image with $\varepsilon=0.9$ with brine saturation $S_b=0.50$. CO₂ is shown in blue and brine in red.

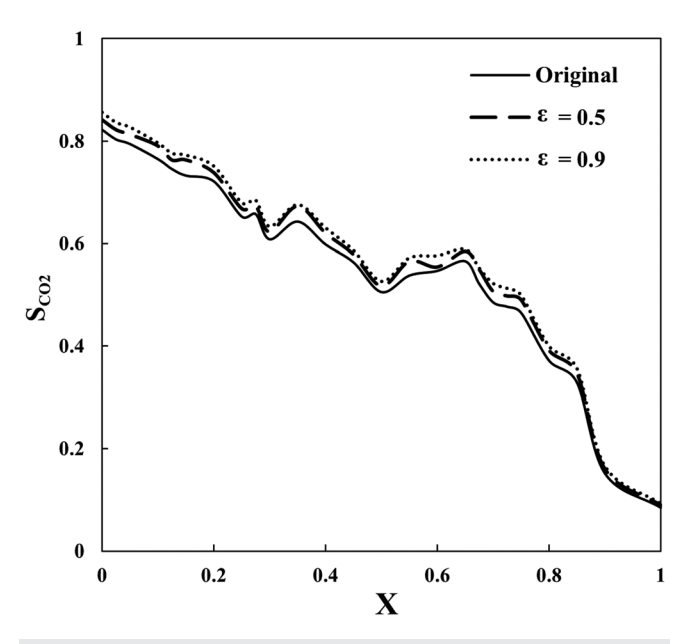


FIG. 9. Saturation profile of CO_2 along the direction x of macroscopic flow at the breakthrough time in the original images of Berea sandstone, as well as two thresholded ones, where X=x/L is the normalized distance of the interface from the inlet, with L being the sample's length in the x direction.

is the actual time, and t_s is the time at which the flow system has reached steady state. Saturation increases linearly with the time as more CO_2 is injected into the pore space, and after the system reaches steady state, it reaches a constant value. More importantly, not only are the three profiles completely similar, the maximum difference

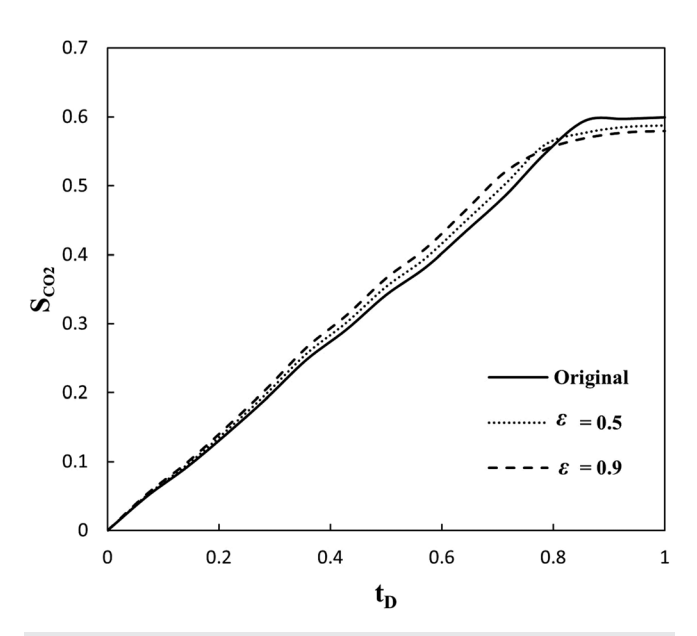


FIG. 10. Comparison of time-dependence of saturation of ${\rm CO_2}$, where $t_D=t/t_{\rm s}$, with $t_{\rm s}$ being the time at which the system reaches steady state, in the original image of the Berea sandstone and its curvelet-transformed images.

between the profile computed in the coarser image with the threshold $\varepsilon=0.9$, and the original image is also practically negligible. The very small differences are due to coarsening and smoothing out some minor pores.

Next, we compare the relative permeabilities, the most important quantity in two-phase flow in porous media. The relative permeability $K_{r,\alpha}$ of fluid α at saturation S_{α} is given by the generalized Darcy's law,

$$v_{\alpha} = -\frac{K_{r,\alpha}(S_{\alpha})K_{e}}{\mu_{\alpha}}\frac{\Delta P_{\alpha}}{\Delta x},$$
 (20)

where v_{α} is the Darcy velocity of fluid phase α , ΔP_{α} is the pressure drop in phase α over a distance Δx , and μ_{α} is the viscosity of phase α . Figure 11 compares the relative permeabilities of brine and CO_2 , computed for the original (uncoarsened) image of the porous medium, with two sets of results computed for the two coarsened images obtained with two distinct thresholds, $\varepsilon=0.5$ and 0.9. The agreement between the three sets of results is excellent.

The high accuracy of the computed relative permeabilities for the thresholded results provided the motivation for making another quantitative comparison between the three sets of results. We show in Fig. 12 the distribution of local $\rm CO_2$ velocities in the original image and compare it with those computed with the thresholded images. All the velocities were normalized by their maximum value. For flow velocities up to the maximum of the distributions, the agreement between the three sets of results is perfect. For flow velocities larger than the maximum, the agreement is good, with all the distributions having the same shape and eventually the same tail.

From a practical viewpoint, the most important quantity in two-phase flow in porous media, in addition to the relative permeability, is the residual saturation Sr of the displaced fluid (here, brine) at CO_2 breakthrough point. We compare in Table II the three computed residual saturations. The maximum difference, computed with $\varepsilon=0.9$, is about 7%.

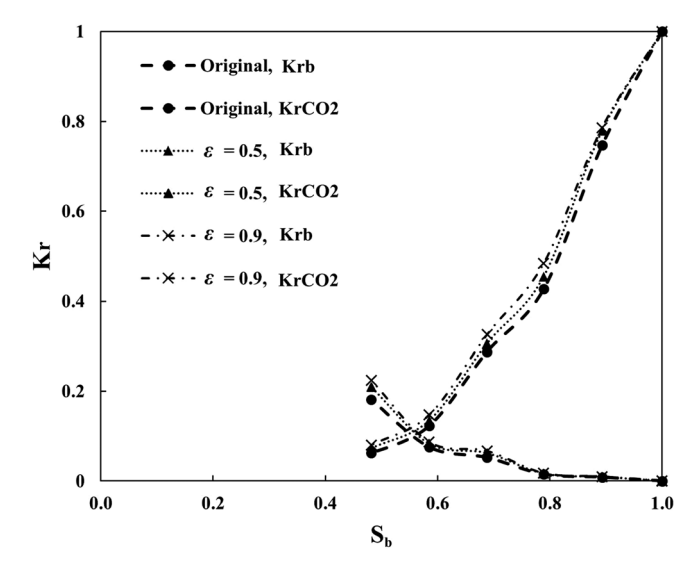


FIG. 11. Relative permeabilities of CO_2 and brine in the Berea sandstone as functions of the brine saturation S_b in the sandstone's original image, as well as its curvelet-thresholded images.

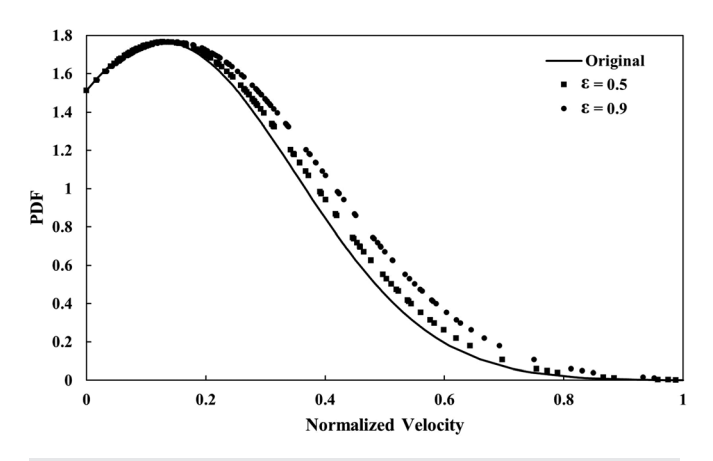


FIG. 12. The probability distribution function (PDF) of the local velocity of CO_2 in the Berea sandstone, normalized by its maximum, in the curvelet-transformed images of the sandstone with two thresholds ε , and its comparison with that of the original image.

C. The regenerated sandstone

We simulated two-phase flow of water and oil in the regenerated sandstone. Once again, water was the wetting fluid. The interfacial tension between the two fluids was 20 mN/m. Oil was injected into the pore space from one face to displace the water that had initially saturated the medium, and the pressure at the opposite face was held constant. Periodic boundary conditions were used in the other four faces.

In terms of their accuracy, all the results for the regenerated sandstone are completely similar to those for the Berea sandstone. Therefore, we present only two main results. Figure 13 presents the saturation of oil vs the dimensionless time t_D , defined earlier. The agreement between the three profiles is excellent.

Figure 14 presents the calculated relative permeabilities to oil and water. Once again, similar to the Berea sandstone, the agreement between the relative permeabilities, computed for the original image, and those for the two coarser images, is excellent.

TABLE II. Comparison of the number of the lattice nodes M, the computation times (in CPU seconds), the speed-up factor S of the computations, and the brine residual saturation Sr, computed with the original and thresholded images.

Berea sandstone	M	Threshold ε	Sr	Time	S
Original image	1 691 443		0.410	140 422	
Curvelet-transformed image	72 978	0.5	0.433	5546	25
Curvelet-transformed image	58 421	0.9	0.441	3953	35
Regenerated sandstone					
Original image	4 140 157		0.149	197 969	
Curvelet-transformed image	609 748	0.5	0.152	25 183	8
Curvelet-transformed image	396 901	0.9	0.153	18 114	11

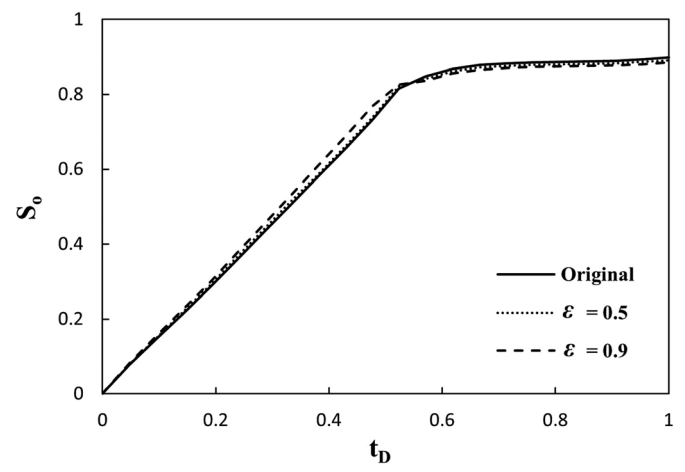


FIG. 13. Comparison of time-dependence of saturation of oil, where $t_D = t/t_s$, with t_s being the time at which the system reaches steady state, in the original image of the regenerated sandstone and its curvelet-transformed images.

D. Efficiency of the computation

It took 196 CPU seconds to compute the CT of the 3D image of the Berea sandstone, while inverse transforming of the coarse images took 203 CPU seconds. The computation time for thresholding the image is insignificant. The corresponding times for the regenerated sandstone, the carbonate medium, and the fractured sample were, respectively, 641, 23, and 8 CPU second. In Table II, we compare the *total* computation times, including the processing of the images, for all the cases, as well as the speed-up factor of the computations.

Table II indicates that the computations with the coarse image of the Berea sandstone that was obtained with the very high threshold of $\varepsilon=0.9$ still produce very accurate results, with a speed-up factor of 35, while those with the thresholds $\varepsilon=0.5$ are accelerated by a factor of 25.

On the other hand, the speed-up factor for the regenerated sandstone is between 8 and 11, still very significant. There are two reasons

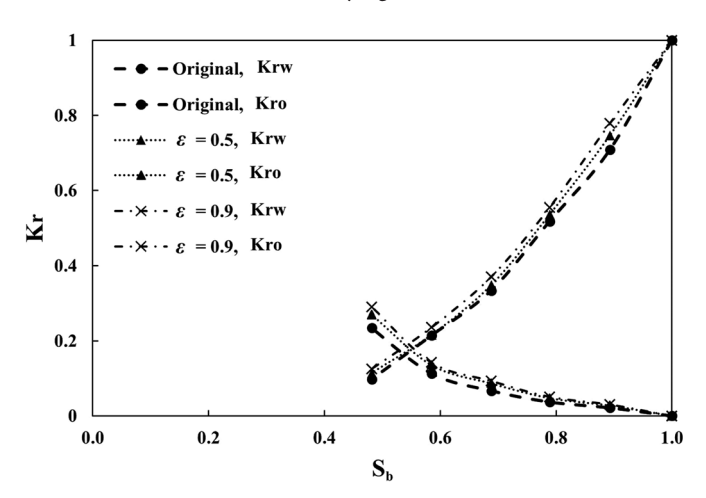


FIG. 14. Relative permeabilities of oil and water in the regenerated sandstone as functions of the brine saturation S_b in the sandstone's original image, as well as its curvelet-thresholded images.

for a smaller speed-up factor for this porous medium. One is that even though the porosities of the two porous media are virtually the same, the regenerated sandstone is more tortuous, hence necessitating larger number of lattice cells to accurately represent the pore space. The second reason is the size of the lattice in the original image of the sandstone, which is roughly 2.5 times larger than that of the Berea sample. Indeed, the speed-up factor for the regenerated sandstone is also by a factor of roughly 3, close to ratio of the sizes of the two lattices.

VII. SUMMARY

Lattice-Boltzmann simulation of multiphase flow in heterogeneous porous media, represented by their high-resolution images, has become practical, but the computations are still intensive and take a long time to carry out. Thus, one must address the issue of high computational cost of such simulations. We proposed a method by which one preprocesses the 3D image and coarsen it by taking it to the curvelet transform space and eliminating those details that do not contribute significantly to multiphase fluid flow. The coarsening is done by thresholding the curvelet coefficients, such that if they are less than a pre-set threshold, their value is set to zero. The resulting sparser representation of the image is then inverse curvelet-transformed and is utilized in the simulation of multiphase flow by the CFLB-MRT approach. We demonstrated that the method accelerates the computations very significantly by a speed-up factor of up to 35.

In a recent paper⁵⁶ in which we solved the Stokes' and the diffusion equations in the images of porous media in order to compute their effective permeability and diffusivity, as well as the flow and concentration fields, we showed that if the two equations are curvelet-transformed and solved in the curvelet-transformed image of the porous medium, one obtains a speed-up factor of four or better, without preprocessing and thresholding the image. The reason is that a coarser computational grid suffices in the curvelet space because many of the CCs of the image are either very small and, thus, do not contribute significantly to simulation of fluid flow, or, due to the aforementioned correlations between the voxels, the CCs are close to those of their neighbors, hence giving rise to a relatively smooth local environment in the curvelet space that makes it possible to use larger lattice blocks.

The same approach may be taken for the LB simulation of fluid flow and transport in the images of porous media. One first determines the CT of the Boltzmann equation that, for example, for a single component in the Bhatnagar, Gross, and Krook approximation 57 is given by 58

$$\frac{\partial f}{\partial t} + \mathbf{v} \cdot \nabla f + \frac{1}{\tau} f = \frac{1}{\tau} g, \tag{21}$$

and similarly for the multicomponent version of the same equation. Here, τ is the relaxation time due to particle collision, and g is the Maxwell–Boltzmann distribution function that, in the 3D space, is given by

$$g = \frac{\rho}{(2\pi RT)^{3/2}} \exp\left[-\frac{(\mathbf{v} - \mathbf{u})^2}{2RT}\right],\tag{22}$$

with *R* and *T* being, respectively, the gas constant and the temperature. The discretized Boltzmann equations used in the simulations can also be curvelet transformed. The curvelet-transformed equation(s) are then solved numerically in the curvelet space, and the numerical results are then inverted back to the real space. Work in this direction will be reported in the near future.

ACKNOWLEDGMENTS

A.A. is grateful to the Public Authority for Applied Education and Training of Kuwait for a Ph.D. scholarship. The authors thank the National Science Foundation for partial support of this work through Grant No. CBET 2000968. We thank Amir Kohanpur and Yu Chen for providing us with the LB code; Senyou An and Vahid Joekar Niasar for providing us with the complete information for the image of the regenerated sandstone and Fig. 2, and Pejman Tahmasebi for helping us to compute the multiple-point connectivity functions. We also thank the anonymous referees whose critical comments contributed significantly to improving the quality of the paper.

AUTHOR DECLARATIONS

Conflict of Interest

The authors declare that they have no conflict of interest.

DATA AVAILABILITY

The data that support the findings of this study are available within the article. The data that support the findings of this study are available from the corresponding author upon reasonable request.

APPENDIX: PARAMETERS OF THE MULTIRELAXATION TIME LATTICE-BOLTZMANN SCHEME

We partition the 19×19 matrix **M** into four submatrices,

$$\mathbf{M} = \begin{bmatrix} \mathbf{M}_1 & \mathbf{M}_2 \\ \mathbf{M}_3 & \mathbf{M}_4 \end{bmatrix}. \tag{A1}$$

Then, the four submatrices are given by

and

Deleting the superscript eq for convenience and brevity, the nineteen entries of the equilibrium moments \mathbf{m}^{eq} are given by

$$m_0 = \rho$$
, $m_1 = -11\rho + 19\rho_0 |\mathbf{v}|^2$, $m_2 = 3\rho - 11\rho_0 |\mathbf{v}|^2 / 2$, (A6)
 $m_3 = \rho_0 v_x$, $m_4 = -2m_3 / 2$, $m_5 = \rho_0 v_y$, (A7)

$$m_6 = -2m_5/3$$
, $m_7 = \rho_0 v_z$, $m_8 = -2m_7/3$, (A8)

$$m_9 = \rho_0(2v_x^2 - v_y^2 - v_z^2), \quad m_{10} = -3m_9/2, \quad m_{11} = \rho_0(v_y^2 - v_z^2),$$
(A9)

$$m_{12} = -m_{11}/2$$
, $m_{13} = \rho_0 v_x v_y$, $m_{14} = \rho_0 v_y v_z$, (A10)

$$m_{15} = \rho_0 v_z v_x, \quad m_{16} = m_{17} = m_{18} = 0,$$
 (A11)

with ρ_0 being the mean fluid density in the system, which is taken to be unity in simulations.

Since the relaxation rates matrix **S** is diagonal, we set $S_{ii} = S_i$ for brevity. Then, the nineteen entries of **S** are given by $S_1 = S_2 = S_9 = S_{10} = S_{11} = S_{12} = S_{13} = S_{14} = S_{15} = -S_{\nu}$, $S_4 = S_6 = S_8 = S_{16} = S_{17} = S_{18} = -S_m$, and $S_0 = S_3 = S_5 = S_7 = 0$, with

$$\frac{1}{S_{\nu}} = \frac{3\nu}{|\mathbf{v}|^2 \Delta t} + 0.5,\tag{A12}$$

where ν is the kinematic viscosity. S_m is given by 59,60

$$S_m = 8 \frac{2 - S_{\nu}}{8 - S_{\nu}}.\tag{A13}$$

The color gradient C, mentioned in the main text, is defined by

$$\mathbf{C} = \frac{3}{|\mathbf{v}|^2 \Delta t} \sum_{i} \omega_i \varphi(\mathbf{x} + \mathbf{v}_i \Delta t, t), \tag{A14}$$

where ω_i are the weight coefficients in the D3Q19 LB model, which are given by

$$\omega_i = \begin{cases} 1/3, & i = 0, \\ 1/18, & i = 1, 2, \dots, 6, \\ 1/36, & i = 7, 8, \dots, 18. \end{cases}$$
 (A15)

Defining a vector **n** by $\mathbf{n} = (n_x, n_y, n_z) = \mathbf{C}/|\mathbf{C}|$, the nonzero entries of \mathbf{m}^s added to the stress-related entries of equilibrium moments \mathbf{m}^{eq} are given by 34

$$m_1^s = -19\sigma |\mathbf{C}|, \quad m_9^s = 0.5\sigma |\mathbf{C}| (2n_z^2 - n_y^2 - n_z^2),$$

 $m_{11}^s = \sigma |\mathbf{C}| (n_y^2 - n_z^2),$ (A16)

$$m_{11}^{s} = \sigma |\mathbf{C}|(n_{y}^{s} - n_{z}^{s}),$$

$$m_{13}^{s} = \sigma |\mathbf{C}|(n_{x}n_{y}), \quad m_{14}^{s} = \sigma |\mathbf{C}|(n_{y}n_{z}), \quad m_{15}^{s} = \sigma |\mathbf{C}|(n_{z}n_{z}).$$
(A17)

REFERENCES

¹J. Bear, Dynamics of Fluids in Porous Media (Elsevier, New York, 1972).

²A. E. Scheidegger, *The Physics of Flow through Porous Media*, 3rd ed. (University of Toronto Press, Toronto, 1974).

³H. I. Meyer, "Pore distribution in porous media," J. Appl. Phys. 24, 510 (1953).
⁴I. Fatt, "The network model of porous media. I. Capillary pressure characteristics," Trans. AIME 207, 155 (1956).

⁵I. Fatt, "The network model of porous media. III. Dynamical properties of networks with tube radius distributions," Trans. AIME 207, 164 (1956).

⁶M. Sahimi, Flow and Transport in Porous Media and Fractured Rock, 2nd ed. (Wiley-VCH, Weinheim, 2011).

⁷M. J. Blunt, Multiphase Flow in Permeable Media: A Pore-Scale Perspective (Cambridge University Press, Cambridge, 2017).

8A. G. Hunt and M. Sahimi, "Flow, transport, and reaction in porous media: Percolation scaling, critical-path analysis, and effective-medium approximation," Rev. Geophys. 55, 993, https://doi.org/10.1002/2017RG000558

⁹H. J. Lemmens, R. Butcher, and P. W. S. K. Botha, "FIB/SEM and SEM/EDX: A new dawn for the SEM in the core lab?," Petrophysics **52**, 452 (2011).

¹⁰S. Sheppard, M. D. Mantle, A. J. Sederman, M. L. Johns, and L. F. Gladden, "Magnetic resonance imaging study of complex fluid flow in porous media: Flow patterns and quantitative saturation profiling of amphiphilic fracturing fluid displacement in sandstone cores," Magn. Reson. Imaging 21, 365 (2003)

¹¹C. H. Arns, M. A. Knackstedt, W. V. Pinczewski, and W. B. Lindquist, "Accurate computation of transport properties from microtomographic images," Geophys. Res. Lett. 28, 3361, https://doi.org/10.1029/2001GL012987 (2001).

¹²C. H. Arns, M. A. Knackstedt, W. V. Pinczewski, and E. Garboczi, "Computation of linear elastic properties from microtomographic images: Methodology and agreement between theory and experiment," Geophysics 67, 1396 (2002).

¹³M. L. Porter, D. Wildenschild, G. Grant, and J. I. Gerhard, "Measurement and prediction of the relationship between capillary pressure, saturation, and interfacial area in a NAPL-water-glass bead system," Water Resour. Res. 46, W08512, https://doi.org/10.1029/2009WR007786 (2010).

¹⁴S. Iglauer, S. Favretto, G. Spinelli, D. Schena, and M. J. Blunt, "X-ray tomography measurements of power-law cluster size distributions for the nonwetting phase in sandstones," Phys. Rev. E 82, 056315 (2010).

¹⁵M. Andrew, H. Menke, M. J. Blunt, and B. Bijeljic, "The imaging of dynamic multiphase fluid flow using synchrotron-based X-ray microtomography at reservoir conditions," Transp. Porous Media 110, 1–24 (2015).

¹⁶S. Berg, H. Ott, S. A. Klapp, A. Schwing, R. Neiteler, N. Brussee, A. Makurat, L. Leu, F. Enzmann, J.-O. Schwarz, M. Kersten, S. Irvine, and M. Stampanoni, "Real-time 3D imaging of Haines jumps in porous media flow," Proc. Natl. Acad. Sci. U. S. A. 110, 3755 (2013).

¹⁷M. Piller, G. Schena, M. Nolich, S. Favretto, F. Radaelli, and E. Rossi, "Analysis of hydraulic, permeability in porous media: From high resolution X-ray tomography to direct numerical simulation," Transp. Porous Media 80, 57 (2009)

- ¹⁸P. Tahmasebi, M. Sahimi, A. H. Kohanpur, and A. J. Valocchi, "Pore-scale simulation of flow of CO₂ and brine in reconstructed and actual 3D rock cores," J. Pet. Sci. Eng. 155, 21 (2017).
- ¹⁹A. H. Kohanpur, M. Rahromostaqim, A. J. Valocchi, and M. Sahimi, "Two-phase flow of CO₂-brine in a heterogeneous sandstone: Characterization of the rock and comparison of the lattice-Boltzmann, pore-network, and direct numerical simulation methods," Adv. Water Resour. 135, 103469 (2020).
- ²⁰S. Bakhshian, Z. Shi, M. Sahimi, T. T. Tsotsis, and K. Jessen, "Image-based modeling of gas adsorption and swelling in high-pressure porous formations," Sci. Rep. 8, 8249 (2018).
- ²¹S. Chen and G. D. Doolen, "Lattice Boltzmann method for fluid flows," Annu. Rev. Fluid. Mech. 30, 329 (1998).
- ²²S. Succi, The Lattice Boltzmann Equations for Fluid Dynamics and Beyond (Oxford University Press, Oxford, 2001).
- ²³A. A. Mohamad, *Lattice Boltzmann Method* (Springer, New York, 2011).
- ²⁴H. Huang, M. C. Sukop, and X.-Y. Lu, Multiphase Lattice Boltzmann Methods: Theory and Application (Wiley, New York, 2015).
- ²⁵R. Fattal, R. Carroll, and M. Agrawala, "Edge-based image coarsening," ACM Trans. Graph. 29, 6 (2009).
- ²⁶E. S. L. Gastal and M. M. Oliveira, "Spectral remapping for image down-scaling," ACM Trans. Graph. 36, 145 (2017).
- 27T. Kogaa and N. Suetake, "Image coarsening by using space-filling curve for decomposition-based image enhancement," J. Visual Commun. Image Representation 24, 806 (2013).
- ²⁸N. Shaffer, B. Martin, and F. Loth, "Cerebrospinal fluid hydrodynamics in type I Chiari malformation," Neurol. Res. 33, 247 (2011).
- 29 P. F. Fischer, G. W. Kruse, and F. Loth, "Spectral element methods for transitional flows in complex geometries," J. Sci. Comput. 17, 81 (2002).
- ³⁰P. H. Valvatne and M. J. Blunt, "Predictive porescale modeling of two-phase flow in mixed wet media," Water Resour. Res. 40, W07406, http://dx.doi.org/ 10.1029/2003WR002627 (2004).
- ³¹T. Ramstad, N. Idowu, C. Nardi, and P.-E. Øren, "Relative permeability calculations from two-phase flow simulations directly on digital images of porous rocks," Transp. Porous Media 94, 487 (2012).
- ³²A. Q. Raeini, M. J. Blunt, and B. Bijeljic, "Direct simulations of two-phase flow on micro-CT images of porous media and upscaling of pore-scale forces," Adv. Water Resour. 74, 116 (2014).
- ³³S. An, H. Yu, and J. Yao, "GPU-accelerated volumetric lattice Boltzmann method for porous media flow," J. Pet. Sci. Eng. 156, 546 (2017).
- ³⁴S. An, Y. Zhan, J. Yao, H. W. Yu, and V. Niasar, "A greyscale volumetric lattice Boltzmann method for upscaling pore-scale two-phase flow," Adv. Water Resour. 144, 103711 (2020).
- 35D. L. Donoho, "Wedgelets: Nearly minimax estimation of edges," Ann. Statist. 27, 859 (1999).
- ³⁶E. Candés, L. Demanent, D. L. Donoho, and L. Ying, "Fast discrete curvelet transforms," Multiscale Model. Simul. 5, 861 (2006).
- ³⁷L. Ying, L. Demanet, and E. Candés, "3D discrete curvelet transform," Proc. SPIE 5914, 591413 (2005).
- ³⁸M. Esmaeili, A. M. Dehnavi, and H. Rabbani, "3D curvelet-based segmentation and quantification of drusen in optical coherence tomography images," J. Electr. Comput. Eng. 2017, 4362603.
- 39Y. Chen, Y. Li, A. J. Valocchi, and K. T. Christensen, "Lattice Boltzmann simulations of liquid CO₂ displacing water in a 2D heterogeneous micromodel at reservoir pressure conditions," J. Contam. Hydrol. 212, 14 (2018).
- ⁴⁰ A. K. Gunstensen, D. H. Rothman, S. Zaleski, and G. Zanetti, "Lattice Boltzman model of immisicle fluids," Phys. Rev. A 43, 4320 (1991).

- ⁴¹J. Tölke, S. Freudiger, and M. Krafczyk, "An adaptive scheme using hierarchical grids for lattice Boltzmann multi-phase flow simulations," Comput. Fluids 35, 820 (2006).
- ⁴²B. Ahrenholz, J. Tölke, P. Lehmann, A. Peters, A. Kaestner, M. Krafczyk, and W. Durner, "Prediction of capillary hysteresis in a porous material using lattice-Boltzmann methods and comparison to experimental data and a morphological pore network model," Adv. Water Resour. 31, 1151 (2008).
- ⁴³J. Tölke, M. Krafczyk, M. Schulz, and E. Rank, "Lattice Boltzmann simulations of binary fluid flow through porous media," Philos. Trans. R. Soc. London A 360, 535 (2002).
- 44H. Chen, S. Chen, and W. H. Matthaeus, "Recovery of the Navier-Stokes equations using a lattice-gas Boltzmann method," Phys. Rev. A 45, R5339 (1992).
- 45Y. Qian, D. d'Humieres, and P. Lallemand, "Lattice BGK models for Navier-Stokes equations," Europhys. Lett. 17, 479 (1992).
- ⁴⁶C. Pan, M. Hilpert, and C. T. Miller, "Lattice Boltzmann simulation of two-phase flow in porous media," Water Resour. Res. 40, W91501, https://doi.org/10.1029/2003WR002120 (2004).
- ⁴⁷A. N. Gorban and D. J. Packwood, "Enhancement of the stability of lattice Boltzmann methods by dissipation control," Physica A 414, 285 (2014).
- ⁴⁸D. d'Humieres, I. Ginzburg, M. Krafczyk, P. Lallemand, and L.-S. Luo, "Multiple-relaxation-time lattice Boltzmann models in three dimensions," Philos. Trans. R. Soc. London A 360, 437 (2002).
- ⁴⁹P. Lallemand and L.-S. Luo, "Theory of the lattice Boltzmann method: Dispersion, dissipation, isotropy, Galilean invariance and stability," Phys. Rev. E 61, 6546 (2000).
- 50 M. Latva-Kokko and D. H. Rothman, "Static contact angle in lattice Boltzmann models of immiscible fluids," Phys. Rev. E 72, 046701 (2005).
- ⁵¹M. A. Knackstedt, A. P. Sheppard, and M. Sahimi, "Pore network modeling of two-phase flow in porous rock: The effect of correlated heterogeneity," Adv. Water Resour. 24, 257 (2001).
- ⁵²J.-L. Starck, E. J. Candés, and D. L. Donoho, "The curvelet transform for image denoising," IEEE Trans. Image Process. 11, 670 (2002).
- 53H. Rabbani, M. Vafadust, and S. Gazor, "Image denoising in curvelet transform domain using Gaussian mixture model with local parameters for distribution of noise-free coefficients," in 4th IEEE/EMBS International Summer School and Symposium on Medical Devices and Biosensors, Cambridge, UK, 19-22 August 2007 (IEEE, 2007).
- 54See A. Verma, https://www.matlabcoding.com/2020/04/curvelet-transform-analysis-and.html for "Curvelet transform analysis and denoising of images using MATLAB;" accessed 30 May 2021.
- 55Y. Liang, "Rock fracture skeleton tracing by image processing and quantitative analysis by geometry features," J. Geophys. Eng. 13, 273 (2016).
- 56 A. Aljasmi and M. Sahimi, "Efficient image-based simulation of flow and transport in heterogeneous porous media: Application of curvelet transforms," Geophys. Res. Lett. 47, e2019GL085671, http://dx.doi.org/10.1029/2019GL085671 (2020).
- ⁵⁷P. L. Bhatnagar, E. P. Gross, and M. Krook, "A model for collision processes in gases. I. Small amplitude processes in charged and neutral one-component systems," Phys. Rev. **94**, 511 (1954).
- 58X. He and L.-S. Luo, "A priori derivation of the lattice Boltzmann equation," Phys. Rev. E 55, R6333 (1997).
- ⁵⁹I. Ginzburg, "Equilibrium-type and link-type lattice Boltzmann models for generic advection and anisotropic-dispersion equation," Adv. Water Resour. 28, 1171 (2005).
- ⁶⁰I. Ginzburg, "Variably saturated flow described with the anisotropic lattice Boltzmann methods," Comput. Fluids 35, 831 (2006).